Materialia 21 (2022) 101328

Contents lists available at ScienceDirect

Materialia

journal homepage: www.elsevier.com/locate/mtla

Coherency strengthening of oblate precipitates extended in the {100} plane of fcc crystals: Modeling and experimental validation

Mohammad Reza Ahmadi[a,*], Bernhard Sonderegger[b], Erwin Povoden-Karadeniz[c], Ahmad Falahati[c], Surya D. Yadav[d], Christof Sommitsch[a], Ernst Kozeschnik[c]

[a] Institute of Material Science, Joining and Forming, Graz University of Technology, Kopernikusgasse 24/I, Graz 8010, Austria
[b] Institute for Engineering Materials - Metals and Alloys, Johannes Kepler University Linz, Altenberger Straße 69, Linz 4040, Austria
[c] Institute of Materials Science and Technology, Vienna University of Technology, Getreidemarkt 9, Vienna 1060, Austria
[d] Department of Metallurgical Engineering, Indian Institute of Technology (BHU), Varanasi 221005, India

ARTICLE INFO

Keyword:
Physical modeling
Non-spherical precipitates
Coherency strengthening
Inconel 718

ABSTRACT

Coherency strengthening plays a major role in precipitation strengthening. The governing mechanism is based on the interaction of dislocations with the elastic strain field induced by the lattice misfit of precipitates and matrix. In the case of non-spherical precipitates, the strain field and corresponding stress field is inhomogeneous and depends on the relative orientation of the particle with respect to the Burger's vector of the dislocation. We evaluate the shear stress increment due to inhomogeneous strain fields around an oblate precipitate and suggested a model for coherency strengthening of oblate precipitates. The corresponding results for the weak and strong strengthening mechanisms demonstrate that shape-depending correction factors need to be incorporated in order to estimate the strength precisely. Afterwards, the proposed model was applied for simulation of precipitation strengthening of Inconel 718. Simulation result shows that, the selection of correct aspect ratio can lead to more accurate yield strength predictions that are close to the experimental results.

1. Introduction

In precipitation strengthening involving coherent precipitates, the lattice misfit between precipitate and matrix produces strain field and a corresponding stress field, which impedes dislocation movement. As a consequence, the yield strength of the material increases. The stress field induces a force on the moving dislocation, which leads to bending of the dislocation line. A precipitate is denoted as *strong precipitate*, when the resistance force is high enough to span the opening angle between the two sides of the dislocation behind a precipitate from π to 0. A *weak precipitate* can bend a straight dislocation from π to a maximum of $2\pi/3$ [1,2].

For spherical and coherent precipitates, Gerold and Haberkorn [3] investigated the resistance force in front of the moving dislocation in a homogeneously strained matrix. Brown and Ham [1] and Ardell [2] used the maximum resistance force of spherical precipitates in front of edge dislocations in each slip plane, F_m, to formulate the shear stress increment, τ_{weak}, of coherent weak particles, when the dislocation line is almost straight as,

$$\tau_{weak} = \frac{2T}{b\lambda_{ss}}\left[\frac{F_m}{2T}\right]^{\frac{3}{2}} \tag{1}$$

where b is the magnitude of the Burgers vector, λ_{ss} is the surface-to-surface distance between two particles. T, the dislocation line tension, is a function of the angle between the dislocation line and its Burgers vector Θ and it is given as,

$$T(\theta) = \frac{Gb^2}{4\pi}\left(\frac{1+\upsilon-3\upsilon(\sin\theta)^2}{1-\upsilon}\right)\ln\left(\frac{r_o}{r_i}\right). \tag{2}$$

where G is the shear modulus and υ is Poisson's ratio, r_o and r_i are the outer and inner cut-off distance [2]. In the following, the symbols T_e and T_s are utilized to denote the dislocation line tensions for edge and screw dislocations, where Θ is $\pi/2$ and 0, respectively.

Ahmadi et al. [4] developed the Eq. (1) for coherency strengthening of weak and shearable precipitates based on isotropic elasticity theory and proposed that,

$$\tau_{weak} = \left(k_{w,\,s}\frac{G^3 b\varepsilon^3(\bar{r})^3}{\lambda_{ss}^2 T}\right)^{\frac{1}{2}}, \tag{3}$$

where $k_{w,s}$ is a constant equal to 592/35 and 9/5 for edge and screw dislocations, respectively, $\bar{r}$ is mean radius of spherical precipitates, ε is the constrained strain produced by the stress free strain of lattice misfit ($\approx 2/3\ \delta$) and δ is lattice misfit [5].

* Corresponding author.
E-mail address: mohammad.ahmadi@tugraz.at (M.R. Ahmadi).

https://doi.org/10.1016/j.mtla.2022.101328
Received 29 October 2021; Accepted 14 January 2022
Available online 16 January 2022

Table 1
Mean Chemical composition of Inconel 718.

	Ni	Al	Co	Cr	C	Fe	Mo	Nb	Ti
%wt	Balance	0.55	0.32	17.6	0.04	20.7	2.92	5.21	1.05

For strong and shearable precipitates they suggested,

$$\tau_{strong} = k_{s,s}\frac{J}{\lambda_{ss}}\left(\frac{T^3 G\varepsilon\bar{r}}{b^3}\right)^{\frac{1}{4}}, \tag{4}$$

where $k_{s,s}$ is a constant equal to $2^{\frac{1}{2}}3^{\frac{3}{8}}$ and 2 for edge and screw dislocations, respectively, and J is a correction factor (equal to 0.8) for the free distance between randomly distributed precipitates in a slip plane in the model of Brown and Ham [1]. In the model of Sonderegger et al. [6] for λ_{ss}, J is considered to be 1.

Serafini et al. [7] and Zhang et al. [8] used the classical strengthening equations suggested for spherical and coherent precipitates to evaluate the coherency strengthening of oblate γ'' precipitates. However, the suggested strengthening equations for non-spherical precipitates need some modification. Nie and Muddle [9–11] analyzed the yield strength increment of incoherent and non-spherical (rod and disc shaped) precipitates by applying stereological methods and assuming that there is no lattice continuity between precipitate and matrix present. Balan et al. [12] applied the suggested model of Nie and Muddle [9–11] for simulation of precipitation strengthening of Inconel 718. They studied the interaction of dislocation in slip plane with the disc-shape γ'' precipitates. Zhu and Starke [13] modified the Orowan strengthening equation [14] based on computer simulations of moving dislocations in the slip plane for different precipitate orientations. Their approach is widely used for yield strength simulations involving non-spherical precipitates [15–17]. However, these two models are only applicable for non-shearable particles.

In the present work, we consider the case where precipitates are oblate, coherent and shearable, which are extended in {100} planes. Furthermore, it is considered that the shear stress of precipitates (Eq. (1)) is a function of the *precipitate free distance* and *the precipitate resistance force*. These conditions resembles with many structural materials, i.e., fcc-structured non-spherical precipitates θ'' in aluminum 2xxx series and γ'' precipitates in Inconel 718, Rene 62 and Udimet 630 [6,18].

In literature, the F_m, λ_{ss} parameters have been derived earlier for both, the spherical [1,2] and non-spherical case [18]. However, these treatments are applicable only to the chemical effect, stacking fault effect, anti-phase boundary and modulus effect because, in these mechanisms, the final shear stress depends on the dislocation length *inside* precipitates. In contrast, for the coherency effect, the final shear stress is a function of the distance of the dislocation from the precipitate center in the slip plane, x, and the distance of the slip plane from the precipitate center, z. In the coherency mechanism, the precipitate resistance force reaches its maximum, *outside* the precipitate limits, which distinguishes this mechanism from other shear strengthening mechanisms. Here, we discuss the coherency effect of oblate precipitates, which are represented by rotational ellipsoids and which are assumed to extend in an fcc matrix in the {100} plane.

2. Material and methods

The suggested model was applied for the simulation of precipitation strengthening of Inconel 718 with the chemical composition as described in Table 1.

In order to evaluate the experimental yield strength, the specimens were first solution heat treated at 985 °C for one hour and then quenched in water. The specimens were then aged at 718 °C for 1, 10, 20, 60 and 80 h. The yield strength of the specimens was then determined three times using a Zwick Z250 tensile testing machine.

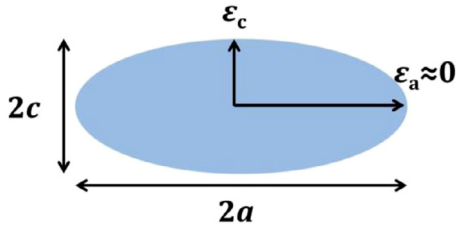

Fig. 1. Thickness (2c) and major axis (2a) of an oblate precipitate with the direction of the strain field.

The microstructure of samples was studied employing transmission electron microscope (TEM) Tecnai F20 model, at 200 kV acceleration voltage. The heat-treated samples were mechanically ground to 0.1 mm. Further, they were then electropolished at −10 °C and 32 V in a solution of 660 ml methanol and 330 ml HNO_3.

Thermokinetic software MatCalc version 5.61 (rel 0.022) was used for the implementation of developed model in order to simulate precipitation hardening along with the mc_ni_v2.011 thermodynamic database and the mc_ni_v2.004 diffusion database.

3. State of the art (theories)

3.1. Free distance between precipitates

Sonderegger et al. [6] have recently derived an expression for the surface-to-surface distance, λ_{ss}, between randomly distributed spherical particles in a matrix, when they are represented in the form of different classes of precipitates having identical sizes, as

$$\lambda_{ss} = \sqrt{\frac{\ln 3}{2\pi\sum_j n_{v,j} r_{v,j}} + \left(2r_{ss}\right)^2} - 2r_{ss}, \tag{5}$$

where

$$r_{ss} = \sqrt{\frac{2}{3}}\frac{\sum_j n_{v,j} r_{v,j}^2}{\sum_j n_{v,j} r_{v,j}}. \tag{6}$$

Herein, $r_{v,j}$ and $n_{v,j}$ are the mean radius and number density of particles in each class, respectively. Later, Sonderegger and Kozeschnik [19] developed a free distance expression for the general case of ellipsoid precipitates. In their model, prolate precipitates are considered to be elongated in <100> directions and oblate precipitates are extended in {100} planes. The proposed coefficients for the shape-depending correction factor to spherical shape are given as,

$$\lambda_{ss,ell} = h^{\frac{1}{6}}\left(\frac{2+h^2}{3}\right)^{\frac{-1}{4}}\lambda_{ss}, \tag{7}$$

$$h = \frac{c}{a}, \tag{8}$$

$$r^3 = a^2 c = h a^3 = c^3 h^{-2}, \tag{9}$$

where a is the half length of major axis, c is half of the rotational axis of the precipitate, h is the aspect ratio and r is the equivalent radius of a sphere with the same volume (see Fig. 1).

In a first step, λ_{ss} in Eq. (1) is replaced by $\lambda_{ss,ell}$ in Eq. (7) to identify the free distance between two oblate precipitates. The distance between two parallel slip planes, which surround a precipitate, is then defined as,

$$2n = 2rh^{-\frac{1}{3}}\sqrt{\frac{2}{3}+\frac{h^2}{3}}, \tag{10}$$

see the sketch in Fig. 2.

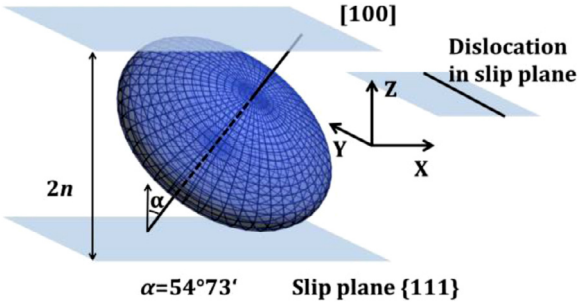

Fig. 2. The interaction between a dislocation and an oblate precipitate sandwiched between two slip planes.

Table 2
Mean interaction force between a dislocation and oblate precipitates in the coherency mechanism.

Dislocation type	Average interaction force F_{coh} b normal to ε_c	b at $(\pi/4)$ to ε_c
Edge	$\frac{4\pi Gb\varepsilon_c}{3\times 6.8}c$	$\frac{4\pi Gb\varepsilon_c}{3\times 2.2}c$
Screw	0	$\frac{4\pi Gb\varepsilon_c}{3\times 4.9}c$

3.2. Resistant force in front of moving dislocation

In the next step, we use the results of Oblak et al. [20], who have evaluated the resistance force F in the inhomogeneous strain field around an oblate precipitate. In their model, precipitates are rotational ellipsoids along the c direction and oblate precipitates are extended in {100} planes. The shape and orientation of oblate precipitates in the Oblak et al. model are in accordance with the model of Sonderegger and Kozeschnik [19] for the free distance between two precipitates. Oblak et al. [20] assumed a tetragonal coherency strain field around the precipitates equal to ε_c in the rotational axes of the oblate in c direction and zero in the a direction (see Fig. 1). They evaluated the precipitate resistance force in front of the moving dislocations with the same assumptions as Gerold and Haberkorn [3], based on the aspect ratio and the angle between the Burgers vector and the rotational precipitate axis $\emptyset$. The analysis of interaction forces, F, delivers the following equations for edge and screw dislocations, respectively,

$$F_1 = F_{edge}\left(\phi=\frac{\pi}{4}\right) = \frac{Gb\varepsilon_c V\left[-6x^4+\sqrt{6}(7+2\upsilon)x^3z+36x^2z^2+\sqrt{6}(3+2\upsilon)xz^3-6z^4\right]}{6\sqrt{6}\pi(1-\upsilon)\left(x^2+z^2\right)^3}, \tag{11}$$

$$F_2 = F_{edge}\left(\phi=\frac{\pi}{2}\right) = \frac{-2Gb\varepsilon_c V xz\left[(1-4\upsilon)x^2-(3+4\upsilon)z^2\right]}{6\pi(1-\upsilon)\left(x^2+z^2\right)^3}, \tag{12}$$

$$F_3 = F_{screw}\left(\phi=\frac{\pi}{4}\right) = \frac{Gb\varepsilon_c V\left[z^2-x^2+\sqrt{2}xz\right]}{\sqrt{6}\pi\left(x^2+z^2\right)^2}, \tag{13}$$

$$F_4 = F_{screw}\left(\phi=\frac{\pi}{2}\right) = 0, \tag{14}$$

and

$$V = \frac{4}{3}\pi c a^2. \tag{15}$$

Oblak et al. [20] proposed mean force values for the different geometries by using Eqs. (11)–(14), with the angle between the dislocation Burger's vector b and precipitate c direction as $\pi/2$ or $\pi/4$, and the dislocations having edge or screw character as listed in Table 2.

4. Model development (calculation)

We distinguish between two coherency weak and strong mechanisms depending on opening angle between the two sides of the dislocation behind a precipitate as discussed in previous sections.

4.1. Coherency weak mechanism

In our further analysis, we assume two types of shearable precipitates. In type one, the angle Ø between the strain fields of precipitates (c direction) with the Burger's vector of the dislocation is $\pi/4$. In type two, Ø is $\pi/2$. We assume that two third of all precipitates belong to type one, while one third belongs to type two (see Fig. 2 in Ref. [18]). On application of the Pythagorean mixture law, as proposed by Brown and Ham [1] and Ardell [2] for shearable components, the final shear stress of oblate precipitates in front of an edge or screw dislocation can be written as,

$$\tau_{weak,obl} = \sqrt{\frac{2}{3}\tau_{type1}^2+\frac{1}{3}\tau_{type2}^2} = \frac{2T}{b\lambda_{ss,ell}}\sqrt{\frac{2}{3}\left(\frac{F_{type1}}{2T}\right)^3+\frac{1}{3}\left(\frac{F_{type2}}{2T}\right)^3}, \tag{16}$$

On substituting the expressions F_1 and F_2 for edge dislocation and F_3 and F_4 for screw dislocation into Eq. (16), the required shear stress for dislocations to cut oblate precipitates becomes,

$$\tau_{weak,obl} = k_w\frac{\left(Gb\varepsilon_c c\right)^{\frac{3}{2}}}{\sqrt{T}b\lambda_{ss,ell}} = k_w\frac{\left(Gb\varepsilon_c r\right)^{\frac{3}{2}}}{\sqrt{T}b\lambda_{ss}}h^{\frac{5}{6}}\left(\frac{2+h^2}{3}\right)^{\frac{1}{4}}, \tag{17}$$

where k_w is a constant equal to 0.6685 and 0.4563 for edge and screw dislocations, respectively. This equation represents the final shear stress for weak oblate precipitates as a function of physical parameters. The parameters entering this equation are the similar as the ones used for spherical precipitates, however, they contain the aspect ratio, now, as an additional parameter reflecting the oblate character.

4.2. Coherency strong mechanism

The shear strength for strong and shearable precipitates can be evaluated analogously on basis of the interaction forces defined in Eqs. (11) – (14). These equations represent the interaction force between edge and screw dislocations with different precipitates as functions of x and z (see Fig. 2). Due to the complex strain field, a dislocation experiences minimum and maximum forces in a specific slip plane (z=const) when it moves and finally cuts the precipitate. Moreover, the force can be attractive or repulsive before or after cutting a precipitate. In the case of the coherency effect, a dislocation must exceed all the critical force values during gliding. The critical force values occur at the points, x, when dF/dx=0. These vary among different slip planes and read,

$$x = mz, \tag{18}$$

where m corresponds to the critical solution of Eqs. (11) –(13), producing absolute maxima for the forces. The numerical solutions for m_1 and m_3 are 0.7276 and 1.1202, respectively, and $m_2 = ((1000^{0.5}-31)/3)^{0.5} = 0.4556$. If we assume υ=1/3, the maximum force in each slip plane reads,

$$F_1 = \frac{4Gb\varepsilon_c ca^2\left[-6m_1^4+\sqrt{6}(7+2\upsilon)m_1^3+36m_1^2+\sqrt{6}(3+2\upsilon)m_1-6\right]}{3\times 6\sqrt{6}(1-\upsilon)\left(1+m_1^2\right)^3z^2} = 0.9565\frac{Gb\varepsilon_c ca^2}{z^2}, \tag{19}$$

$$F_2 = \frac{-4Gb\varepsilon_c ca^2m_2\left[(1-4\upsilon)m_2^2-(3+4\upsilon)\right]}{3\times 3(1-\upsilon)\left(1+m_2^2\right)^3z^2} = 0.7593\frac{Gb\varepsilon_c ca^2}{z^2}, \tag{20}$$

$$F_3 = \frac{4Gb\varepsilon_c ca^2\left[1 - m_3^2 + \sqrt{2}m_3\right]}{3 \times \sqrt{6}\left(m_3^2 + 1\right)^2 z^2} = 0.1424\frac{Gb\varepsilon_c ca^2}{z^2}, \quad (21)$$

In the shearing and strong coherency strengthening mechanism, i.e., when the coherent precipitates become large, the maximum resistance force of precipitates can reach values comparable to that of the non-shearing (Orowan) mechanism, which is

$$F_{max} \cong 2T. \quad (22)$$

This condition applies to dislocations located in specific slip planes between $z_{min} \le z \le z_{max}$. z_{min} and z_{max} are the most distant slip planes from the center $z = 0$ of the precipitate, where this criterion holds. For the dislocations located outside $z_{min} \le z \le z_{max}$, weaker strengthening mechanisms operate. Using a similar method as the one applied for spherical precipitates [1,2], we neglect the effect of any weaker strengthening contribution occurring in slip planes outside z_{min} and z_{max} [21]. The critical z values are obtained either in the area surrounded by the two bounding slip planes defined in Fig. 2 or outside the precipitate, depending on the precipitate size and ε_c. $z_{1,max}$, $z_{2,max}$ and $z_{3,max}$ are identified by substituting Eqs. (19) –(21) into Eq. (22) with,

$$z_{1\ max} = \sqrt{0.4783\frac{Gb\varepsilon_c ca^2}{T_e}}, \quad (23)$$

$$z_{2,max} = \sqrt{0.3797\frac{Gb\varepsilon_c ca^2}{T_e}}, \quad (24)$$

$$z_{3,max} = \sqrt{0.0712\frac{Gb\varepsilon_c ca^2}{T_s}}. \quad (25)$$

We next introduce a function $g(z)$, which designates the fraction of $|z_{max} - z_{min}|$ with respect to the height of the precipitate in slip plane n which is,

$$g(z) = \frac{z_{max} - z_{min}}{2n}. \quad (26)$$

The function $g(z)$ is equal to one when $|z_{max} - z_{min}| = 2n$ for oblate precipitates or $|z_{max} - z_{min}| = 2r$ for spherical precipitates. In this case, the shear stress of oblate precipitates is $\tau_{strong,obl} = (2T/(b\lambda_{ss,ell}))$. The shear stress of strong and shearable oblate precipitates is then expressed as

$$\tau_{strong,obl} = J\frac{2T}{b\lambda_{ss,ell}}\sqrt{\frac{2}{3}g(z_{type1}) + \frac{1}{3}g(z_{type2})}, \quad (27)$$

By substituting Eqs. (23) –(25) into Eq. (26), and then into Eq. (27), the required shear stress for cutting strong precipitates becomes

$$\tau_{strong,obl} = k_s\frac{J}{\lambda_{ss,ell}}\left(\frac{2+h^2}{3}\right)^{\frac{-1}{4}}\left(\frac{T^3G\varepsilon_c\ c}{b^3}\right)^{\frac{1}{4}} = k_s\frac{J}{\lambda_{ss}}\left(\frac{T^3G\varepsilon_c r}{b^3}\right)^{\frac{1}{4}}, \quad (28)$$

where k_s is a constant equal to 1.6327 and 0.8435 for edge and screw dislocations, respectively.

5. Results and discussion

The normalized shear stress for cutting oblate precipitates in the coherency mechanism for weak and strong precipitates is shown in Fig. 3. When the lattice misfit between precipitate and matrix is dissimilar in different crystallographic directions, the precipitate prefers to extend in direction(s) with lower lattice misfit. For the oblate precipitates described in this work, the lattice misfit in a direction is assumed to be small compared to the misfit in c direction. Consequently, the precipitate extends mainly in the a direction, which produces a lower strain level in the matrix. Simultaneously, precipitate growth in c direction is limited. In this case, the precipitate resistance force depends on the precipitate thickness and lattice misfit in c direction. When the aspect ratio is varied from one to zero and with the assumption of constant precipitate phase fraction, the strain field around the precipitate gradually decreases, simultaneously with the precipitate resistance force. This decrease is compensated, however, by the counteracting effect of free distance between two oblate particles on shear stress. For the strong coherency effect, the final shear stress becomes independent of the aspect ratio h. As described in simplified Eq. (28), the strong coherency effect is a function of equivalent radius r and surface-to-surface distance between randomly distributed spherical particles λ_{ss}. This means that the normalized shear stress does not change if the fraction of precipitates is constant (see Fig. 3). In the weak mechanism, the precipitate resistance force has a more prominent effect on strengthening compared to the free distance effect. In summary, the final shear stress in the weak mechanism depends strongly on the aspect ratio. It can also be deduced that the shear stress decreases with decreasing aspect ratio.

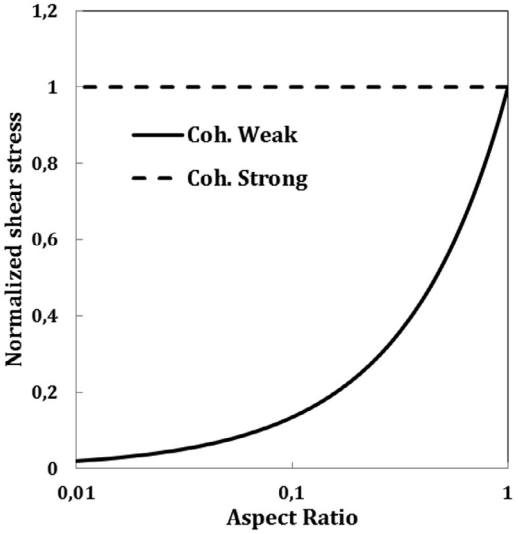

Fig. 3. Normalized shear stress for weak and strong coherency effect based on Eqs. (17) and (28) as a function of the aspect ratio h.

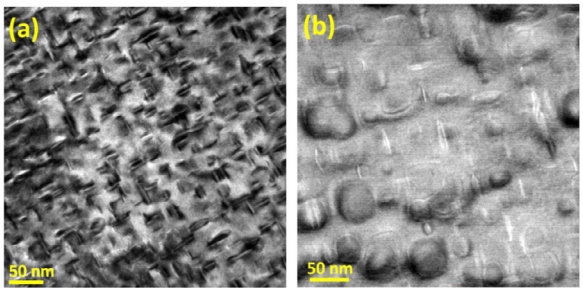

Fig. 4. TEM microstructure of Inconel 718 after (a) 20 h and (b) 60 h aging at 718 °C. The direction of electron beam is [001].

The suggested model was applied for the evaluation of final yield strength of Inconel 718 including oblate γ'' precipitates during aging. This model was implemented in MatCalc 5.61 (rel 0.022) in order to simulate the precipitation strengthening. Beside coherency effect, other strengthening mechanism such as anti-phase boundary, modulus and interfacial effects were also considered for evaluation of final yield strength. The input parameters used for simulation of precipitation strengthening of Inconel 718 are given in Table 3.

Fig. 4 demonstrates distribution and size of oblate γ'' precipitates in microstructure of Inconel 718 after 20 and 60 h aging at 718 °C. As it is shown in this figure, the size of oblate γ'' precipitates, increases by aging time.

Table 3
Used parameters for simulation of precipitation strengthening of Inconel 718.

Parameters	Values	Refs.
G (GPa) (Shear modulus of matrix)	75.2	[22]
G_P (GPa) (Shear modulus of γ'' precipitate)	81.65	[7,23]
M (Taylor factor)	2.6	[24]
γ_{IF} (Jm^{-2})	0.22	MatCalc thermodynamic database
γ_{APB} (Jm^{-2})	0.296	[25]
δ (linear misfit in C direction)	0.0286	[26]
r_i (inner cut-off distance)	2b	
υ (Poisson's ratio)	0.33	
b Burgers vector (nm)	0.254	

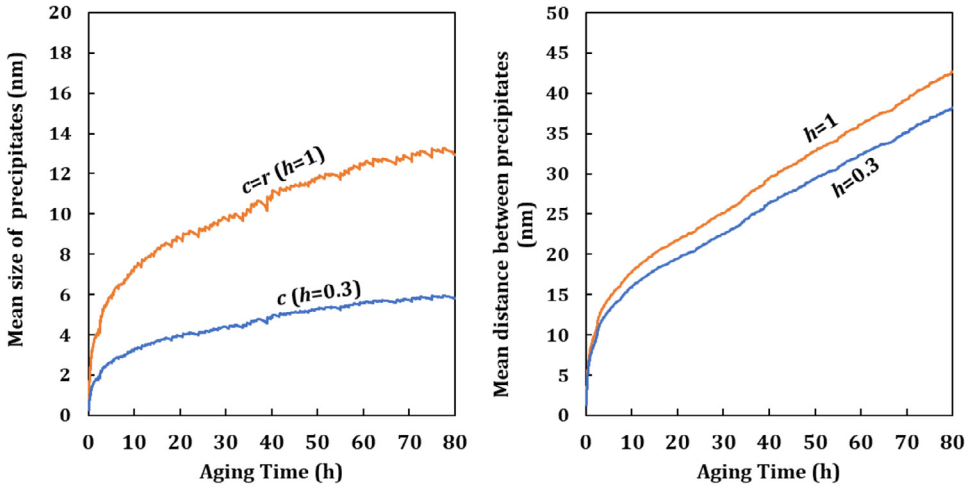

Fig. 5. Simulation results of (a) mean size of γ'' precipitates and (b) mean distance between γ'' precipitates during aging at 718 °C, when the aspect ratios is $h = 0.3$ and $h = 1.0$.

Simulation results also confirms the changes of radius and free distance between precipitates during aging. Fig. 5 shows gradual increase of precipitate size (Fig. 5a) and free distance (Fig. 5b) between γ'' precipitates with aging time. As can be seen in Fig. 5(a), the c-value (half of the rotational axis of the precipitate) decreases more than twofold as the aspect ratio h varies from 1.0 to 0.3. Analogously, the free distance between the precipitates decreases slightly as the aspect ratio h decreases (See Fig. 5(b)). Changes of c and h-values on coherency strengthening of Inconel 718 as described in Eqs. (17) and (28) is demonstrated in Fig. 6(a). This figure confirms that decreasing of c-value can effectively decrease coherency strengthening, although decreasing of the free distance between precipitates due to the changes of h-value can slightly improve coherency strengthening.

The anti-phase boundary (APB) has also a significant impact on the precipitation strengthening of Inconel 718. Similar to the coherency effect, this mechanism is divided to weak and strong shearing mechanisms which are described in Refs. [4,18] as,

$$\tau_{\mathrm{APB,weak}} = \frac{2T}{b\lambda_{\mathrm{ss,ell}}}\left[\frac{\gamma_{\mathrm{APB}}\bar{\omega}_{\mathrm{eq}}}{T}\right]^{\frac{3}{2}} - \frac{16}{3\pi}\frac{\gamma_{\mathrm{APB}}\bar{\omega}_{\mathrm{eq}}^2}{b{\lambda_{\mathrm{ss,ell}}}^2} \tag{29}$$

for weak mechanism and,

$$\tau_{\mathrm{APB,strong}} = \left(\frac{2wT}{\pi b\lambda_{\mathrm{ss,ell}}}\right)\left(\frac{\pi^2\gamma_{\mathrm{APB}}\bar{\omega}_{\mathrm{eq}}}{4wT} - 1\right)^{\frac{1}{2}}, \tag{30}$$

for strong mechanism, Herein $\bar{\omega}_{\mathrm{eq}}$ can be defined as,

$$\bar{\omega}_{\mathrm{eq}} = \frac{\pi c}{12}\left[P_e\left(\sqrt{\frac{3}{2+h^2}} + 2\sqrt{\frac{6}{1+5h^2}}\right) + P_s\left(\frac{1}{h} + 2\sqrt{\frac{2}{1+h^2}}\right)\right], \tag{31}$$

where γ_{APB} is the anti-phase boundary energy of the precipitate, w is a constant (≈2.8), and P_e and P_s are the fractions of edge and screw dislocations in the matrix, respectively. Fig. 6(b) expresses the APB strengthening of γ'' precipitates at $h = 1.0$ and $h = 0.3$ as described in Eqs. (29)–(31).

The increase of precipitation strengthening due to the modulus and interfacial effects is similar to the APB effect and described in Refs. [4,18]. As described in Ref. [27], the contribution of these two mechanisms to the precipitation strengthening is negligible and, for simplicity, the strengthening equations of modulus and interfacial effects are not mentioned in this paper [28]. However, the contribution of all strengthening mechanisms, including modulus and interfacial effects to the precipitation strengthening of Inconel 718 is exhibited in Fig. 6(c). This figure shows combination of different strengthening weak and strong mechanisms. Beside shearing mechanism, this figure shows the ultimate shear stress relate to the non-shearable Orowan mechanism. In this mechanism, the opening angle between the two sides of the dislocation behind a precipitate reaches to 0. The dislocations leave the precipitates after forming a loop around them. The strengthening equation for non-shearing precipitates as a function of aspect ratio is proposed in Ref. [18] as,

$$\tau_{\mathrm{Or.}} = \frac{Gb}{2\pi\sqrt{1-\upsilon}}\frac{1}{\lambda_{\mathrm{ss,ell}}}\ln \left\{\frac{\pi c}{6r_i}\left[P_e\left(\sqrt{\frac{3}{2+h^2}} + \sqrt{\frac{3}{h^2}+\frac{3}{2+h^2}}\right) + P_s\left(\sqrt{\frac{1}{h^2}+\frac{9}{2+h^2}} + \frac{1}{h}\right)\right]\right\}, \tag{32}$$

When the h-value is equal to 1, the non-shearable Orowan mechanism will be controlling mechanism after 25 h of aging due to the lower strengthening values than shearable weak and strong mechanisms. This means that the precipitates are not shearable after 25 h of aging. How-

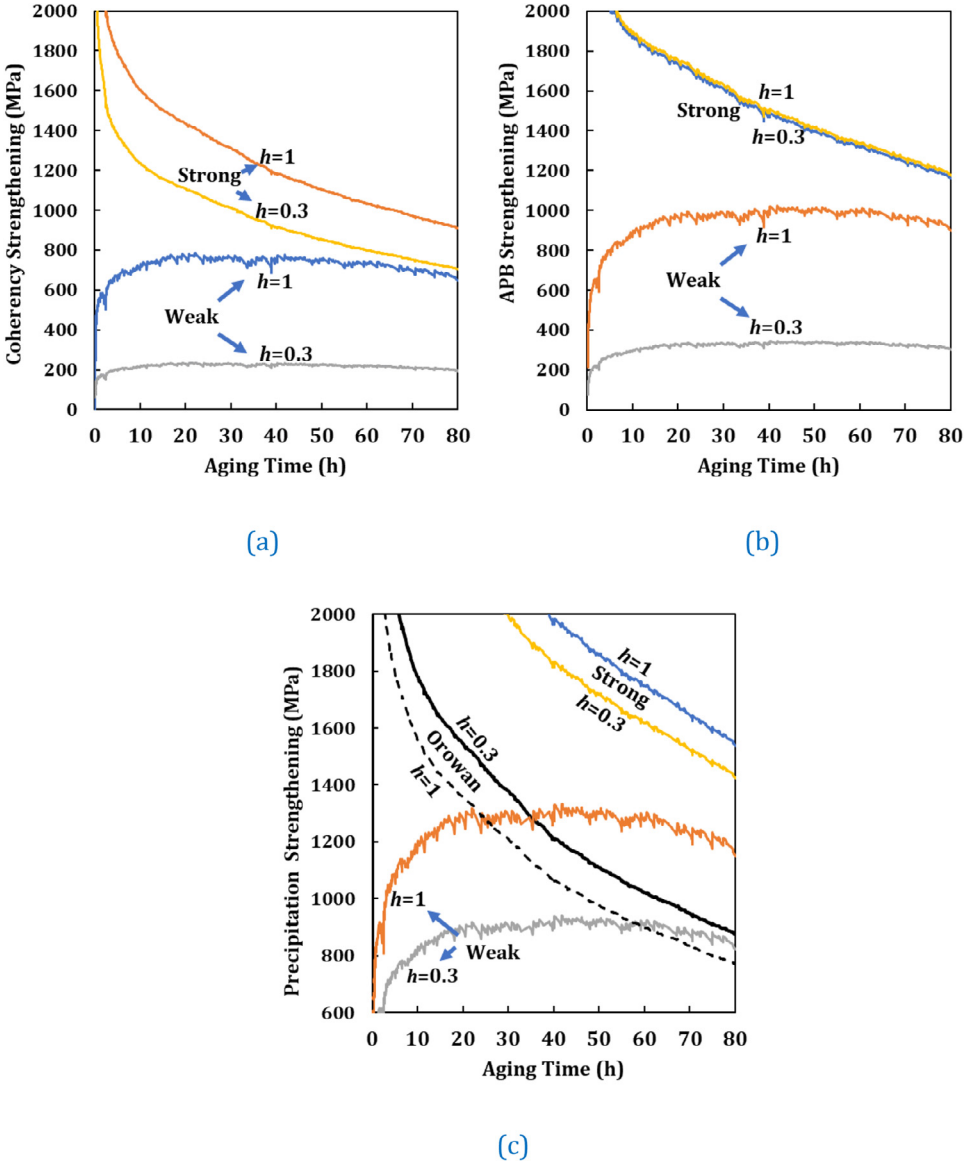

Fig. 6. Contribution of (a) coherency strengthening (b) anti-phase boundary strengthening (c) precipitation strengthening of Inconel 718 during aging at 718 °C, when the aspect ratios is $h = 0.3$ and $h = 1.0$.

ever, the operative strengthening mechanism will be weak and shearable, if we correctly choose an h-value of equal to or less than 0.3.

Fig. 7 shows simulation result of precipitation hardening of Inconel 718 during aging at 718 °C. As can be seen in Fig. 7(a), the application of the classical strengthening equations considering $h = 1$ (spherical precipitates) leads to an overestimation of the precipitation strengthening of 1300 MPa, which is ~70% higher than the real condition when h varies between 0.1 and 0.3. As it is shown in Fig. 7(a), transformation from coherency weak mechanism to non-shearing mechanism occurs after 25 h, while this transformation occurs after 50 h when $h = 0.5$. Simulation results express operating weak strengthening mechanism for γ'' precipitates for lower h-values up to 80 h aging.

In early aging time, when the precipitates are tiny, the operative strengthening mechanism is weak and shearable, while in late aging time precipitates become thick and operative strengthening mechanism varies to non-shearing mechanism.

Final yield strength in metallic matrix is contribution of intrinsic, grain size, solid solution and precipitation effects [4,29,30]. The share of intrinsic, and grain size effects in final yield strength of Inconel 718 is $\sigma_{y,i}$ = 21.8 MPa [31]and $\sigma_{y,g}$ = 35.3 MPa, respectively. The effect of grain size on final yield strength depends on D which is the grain diameter and constant k_{lock} which is 0.158 MPa $m^{1/2}$ for nickel-base superalloys. This equation is described in Ref. [27] as,

$$\sigma_{y,g} = \frac{k_{lock}}{\sqrt{D}} \tag{33}$$

Solid solution strengthening of the individual alloying elements is described in Ref. [32] as,

$$\sigma_{y,s} = \left[\sum_i \left(k_{s,i} C_i^{0.5}\right)^2\right]^{0.5} \tag{34}$$

where, $k_{s,i}$ is a strengthening constant for solute i and C_i is the concentration of solute i. Mishima et al. [33] defined $k_{s,i}$ values for different alloying elements in nickel-base alloys as described in table Table 4. These values were implemented in MatCalc software.

The simulation result of solid solution strengthening using MatCalc is $\sigma_{y,s}$ = 268 MPa before again which decreases to the $\sigma_{y,s}$ = 252 MPa after 80 h aging. This decrease is due to the migration of alloying elements from matrix to precipitates [26,27].

The final yield strength σ_y of different strengthening mechanisms is linearly added up of intrinsic effect, grain size effect, solid solution strengthening, and precipitation strengthening, which, is demonstrated

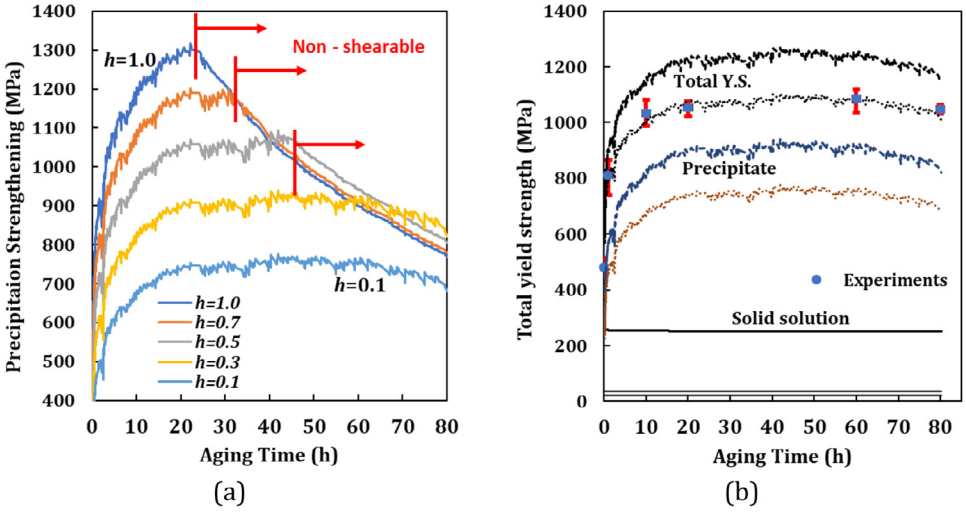

Fig. 7. (a) Simulation of precipitation strengthening of Inconel 718 at different aspect ratios of the oblate γ'' precipitates during aging at 718 °C (b) simulation of yield strength in Inconel 718, considering intrinsic, grain boundaries, solid solution and precipitation strengthening at 0.1 and 0.3 aspect ratios of the oblate γ'' precipitates during aging at 718 °C and its comparison with experimental results.

Table 4
Strengthening constants ($k_{s,i}$)of different alloying elements in Ni [33].

Alloying element	Al	Co	Cr	C	Fe	Mo	Nb	Ti
Strengthening constant (MPa atomic fraction$^{-1/2}$)	225	39.4	337	1061	153	1015	1183	775

in Fig. 7(b) [4,29,30]. As it is shown in this figure, the precipitation strengthening of Inconel 718 is strongly depends on the aspect ratio. According to the image analysis of TEM, the aspect ratio of oblate γ'' precipitates varies between 0.1 and 0.3 in this study,

6. Conclusion

In the present study, we derive a model to evaluate the coherency strengthening effect of oblate precipitates. The proposed equations for the final yield strength are formulated in terms of physical parameters only. Our treatment suggests that one can use the classical strengthening equations of spherical precipitates for oblate precipitates by application of a correction factor. We finally observe that, when the precipitate shape deviates from spherical to oblate, the weak strengthening effect for shearable precipitates decreases, whereas the strengthening effect for strong shearable precipitates is independent of the aspect ratio.

The suggested model was applied for simulation of precipitation strengthening of Inconel 718 containing oblate γ'' precipitates. The simulation results show that modification of aspect ratio based on experimental results can significantly improve accuracy of final yield strength.

Declaration of Competing Interest

Declaration of Competing Interest The authors declare that they have no known competing financial interests or personal relationships that could have appeared to influence the work reported in this paper.

Acknowledgment

The authors gratefully acknowledge the financial support under the scope of the COMET program within the K2 Center “Integrated Computational Material, Process and Product Engineering (IC-MPPE)” (Project No 859480). This program is supported by the Austrian Federal Ministries for Transport, Innovation and Technology (BMVIT) and for Digital and Economic Affairs (BMDW), represented by the Austrian research funding association (FFG), and the federal states of Styria, Upper Austria and Tyrol.

The authors acknowledge the Austrian Federal Government (in particular from the Bundesministerium für Verkehr, Innovation und Technologie and the Bundesministerium für Wirtschaft, Familie und Jugend) and the Styrian Provincial Government, represented by Österreichische Forschungsförderungsgesellschaft mbH and by Steirische Wirtschaftsförderungsgesellschaft mbH, within the research activities of the K2 Competence center on “Integrated Research in Materials, Processing and Product Engineering”, operated by the Materials Center Leoben Forschung GmbH in the framework of the Austrian COMET Competence center Programme.

References

[1] L. Brown, R.K. Ham, Strengthening Methods in Crystals, Elsevier, Amesterdam, The Netherlands, 1971.
[2] A.J. Ardell, Precipitation hardening, Metall. Trans. A 16A (1985) 2131–2165, doi:10.1016/B978-0-08-098204-5.00017-1.
[3] V. Gerold, H. Haberkorn, On the critical resolved shear stress of solid solutions containing coherent precipitates, Phys. Status Solidi 16 (1966) 675–684, doi:10.1002/pssb.19660160234.
[4] M.R. Ahmadi, E. Povoden-Karadeniz, K.I. Öksüz, A. Falahati, E. Kozeschnik, A model for precipitation strengthening in multi-particle systems, Comput. Mater. Sci. 91 (2014) 173–186, doi:10.1016/j.commatsci.2014.04.025.
[5] J.D. Eshelby, The determination of the elastic field of an ellipsoidal inclusion, and related problems, Proc. R. Soc. A Math. Phys. Eng. Sci. 241 (1957) 376–396, doi:10.1098/rspa.1957.0133.
[6] B. Sonderegger, I. Holzer, E. Kozeschnik, C. Sommitsch, Particle distance distributions and their effect on precipitation strengthening, Comput. Methods Mater. Sci. 11 (2011) 148–153.
[7] A. Serafini, G. Angella, C. Malara, M.F. Brunella, Mechanical and microstructural characterization of AF955 (UNS N09955) nickel-based superalloy after different heat treatments, Metall. Mater. Trans. A Phys. Metall. Mater. Sci. 49 (2018) 5339–5352, doi:10.1007/s11661-018-4876-9.
[8] S. Zhang, X. Lin, L. Wang, X. Yu, Y. Hu, H. Yang, L. Lei, W. Huang, Strengthening mechanisms in selective laser-melted Inconel718 superalloy, Mater. Sci. Eng. A 812 (2021) 141145, doi:10.1016/j.msea.2021.141145.
[9] J.F. Nie, B.C. Muddle, Strengthening of an Al-Cu-Sn alloy by deformation-resistant precipitate plates, Acta Mater. 56 (2008) 3490–3501, doi:10.1016/j.actamat.2008.03.028.
[10] J.F. Nie, B.C. Muddle, Microstructural design of high-strength aluminum alloys, J. Phase Equilibria 19 (1998) 543–551, doi:10.1361/105497198770341734.
[11] J.F. Nie, Effects of precipitate shape and orientation on dispersion strengthening in magnesium alloys, Scr. Mater. 48 (2003) 1009–1015, doi:10.1016/S1359-6462(02)00497-9.
[12] A. Balan, M. Perez, T. Chaise, S. Cazottes, D. Bardel, F. Corpace, F. Pichot, A. Deschamps, F. De Geuser, D. Nelias, Precipitation of γ'' in Inconel 718 alloy from microstructure to mechanical properties, Materialia 20 (2021) 101187, doi:10.1016/j.mtla.2021.101187.
[13] A.W. Zhu, E.A. Starke, Strengthening effect of unshearable particles of finite size: a computer experimental study, Acta Mater. 47 (1999) 3263–3269, doi:10.1016/S1359-6454(99)00179-2.

[14] E. Orowan, Discussion on internal stresses, Symp. Intern. Stress. Met. Alloy. Sess. III Discuss. Inst. Met. London, Engl. (1948) 451–453.
[15] I.N. Khan, M.J. Starink, J.L. Yan, A model for precipitation kinetics and strengthening in Al-Cu-Mg alloys, Materials Science and Engineering A 472 (2008) 66–74.
[16] G. Liu, G.J. Zhang, X.D. Ding, J. Sun, K.H. Chen, Modeling the strengthening response to aging process of heat-treatable aluminum alloys containing plate/disc- or rod/needle-shaped precipitates, Mater. Sci. Eng. A 344 (2003) 113–124, doi:10.1016/S0921-5093(02)00398-2.
[17] M. Song, Modeling the hardness and yield strength evolutions of aluminum alloy with rod/needle-shaped precipitates, Mater. Sci. Eng. A 443 (2007) 172–177, doi:10.1016/j.msea.2006.08.025.
[18] M.R. Ahmadi, B. Sonderegger, E. Povoden-Karadeniz, A. Falahati, E. Kozeschnik, Precipitate strengthening of non-spherical precipitates extended in ⟨100⟩ or {100} direction in fcc crystals, Mater. Sci. Eng. A (2014) 590, doi:10.1016/j.msea.2013.10.043.
[19] B. Sonderegger, E. Kozeschnik, Particle strengthening in fcc crystals with prolate and oblate precipitates, Scr. Mater. 66 (2012) 52–55, doi:10.1016/j.scriptamat.2011.10.003.
[20] J.M. Oblak, D.S. Duvall, D.F. Paulonis, An estimate of the strengthening arising from coherent, tetragonally-distorted particles, Mater. Sci. Eng. 13 (1974) 51–56.
[21] M.R. Ahmadi, E. Povoden-Karadeniz, B. Sonderegger, K.I. Öksüz, A. Falahati, E. Kozeschnik, A model for coherency strengthening of large precipitates, Scr. Mater. 84–85 (2014) 47–50, doi:10.1016/j.scriptamat.2014.04.019.
[22] V. Gelbov, F. Lobkowicz, Deformation of the cryostat cold vessel under the load of the EM calorimeter, ATLAS Intern. Note. LARG-NO-030, 12 December (1995), 1–12.
[23] S. Dai, W. Liu, First-principles study on the structural, mechanical and electronic properties of δ and γ'' phases in Inconel 718, Comput. Mater. Sci. 49 (2010) 414–418, doi:10.1016/j.commatsci.2010.05.031.
[24] B. Clausen, T. Lorentzen, T. Leffers, Self-consistent modelling of the plastic deformation of f.c.c. polycrystals and its implications for diffraction measurements of internal stresses, Acta Mater. 46 (1998) 3087–3098.
[25] J. Oblak, D. Paulonis, D. Duvall, Coherency strengthening in Ni base alloys hardened by DO_{22} γ'' precipitates, Metall. Mater. Trans. B 5 (1974) 143–153.
[26] M.R. Ahmadi, M. Rath, E. Povoden-Karadeniz, S. Primig, T. Wojcik, A. Danninger, M. Stockinger, E. Kozeschnik, Modeling of precipitation strengthening in Inconel 718 including non-spherical γ" precipitates, Model. Simul. Mater. Sci. Eng. (2017) 25, doi:10.1088/1361-651X/aa6f54.
[27] M.R. Ahmadi, E. Povoden-Karadeniz, L. Whitmore, M. Stockinger, A. Falahati, E. Kozeschnik, Yield strength prediction in Ni-base alloy 718Plus based on thermo-kinetic precipitation simulation, Mater. Sci. Eng. A 608 (2014) 114–122, doi:10.1016/j.msea.2014.04.054.
[28] M.R. Ahmadi, L. Whitmore, E. Povoden-Karadeniz, M. Stockinger, A. Falahati, E. Kozeschnik, Simulation of yield strength in Allvac®718Plus™, Adv. Mater. Res. 922 (2014) 7–12, doi:10.4028/www.scientific.net/AMR.922.7.
[29] P. Lang, T. Weisz, M.R. Ahmadi, E. Povoden-Karadeniz, A. Falahati, E. Kozeschnik, Thermo-kinetic simulation of the yield strength evolution of AA7075 during natural aging, Adv. Mater. Res. 922 (2014) 406–411, doi:10.4028/www.scientific.net/AMR.922.406.
[30] L. Whitmore, M.R. Ahmadi, M. Stockinger, E. Povoden-Karadeniz, E. Kozeschnik, H. Leitner, Microstructural investigation of thermally aged nickel-based superalloy 718Plus, Mater. Sci. Eng. A 594 (2014) 253–259, doi:10.1016/j.msea.2013.11.037.
[31] T.P. Gabb, J. Telesman, A. Banik, E. Mcdevitt, Use of slow strain rate tensile testing to assess the ability of several superalloys to resist environmentally-assisted intergranular cracking,8th International Symposium on Superalloy 718 and Derivatives (2020) 639–654.
[32] M.Z. Butt, K.M. Hashmi, P. Feltham, Solid-solution hardening in hexagonal alloys, J. Phys. D Appl. Phys. 11 (1981) 275–279, doi:10.1088/0305-4608/11/11/003.
[33] Y. Mishima, S. Ochiai, N. Hamao, M. Yodogawa, T. Suzuki, Solid solution hardening of nickel–role of transition metal and B-subgroup solutes, Trans. Jpn. Inst. Met. 27 (1986) 656–664, doi:10.2320/matertrans1960.27.656.